Subrainband Structure and Dynamic Characteristics in the Principal Rainband of Typhoon Hagupit (2008)

XIAOWEN TANG

School of Atmospheric Sciences, Nanjing University, Nanjing, China

WEN-CHAU LEE

National Center for Atmospheric Research, Boulder, Colorado

MICHAEL BELL

Colorado State University, Fort Collins, Colorado

ABSTRACT

The principal rainband in tropical cyclones is currently depicted as a solitary and continuous precipitation region. However, the airborne radar observations of the principal rainband in Typhoon Hagupit (2008) reveal multiple subrainband structures. These subbands possess many characteristics of the squall lines with trailing stratiform in the midlatitudes and are different from those documented in previous principal rainband studies. The updraft and reflectivity cores are upright and elevated. The updraft is fed by a low-level radial outflow from the inner side. The tangential wind speed shows a clear midlevel jet on the inner side of the reflectivity core. Except for the structural similarities, the dynamics of the subbands is also similar to the squall lines. The local environment near the subbands shows little convective inhibition, modest instability, and vertical wind shear. The temperature retrieval shows a cold pool structure in the stratiform precipitation region. The estimated vertical wind shear induced by the cold pool is close to that of the local environment. The structural and dynamic similarities to the squall lines imply that the variation of principal rainbands is subjected to convective-scale dynamics related to the local environment in addition to storm-scale dynamics. The subbands show positive impacts to the vortex intensity in terms of potential vorticity redistribution and absolute angular momentum advection. The positive impacts are closely related to specific structural characteristics of the subbands, which suggests the importance of understanding the convective-scale structure and dynamics of the principal rainband.

1. Introduction

Understanding and predicting tropical cyclone (TC) intensity change has been a long-standing challenge in TC research. Factors related to TC intensity change include both environmental conditions and internal dynamics. TC internal dynamics are manifested in various TC structures and their evolutions, and understanding the latter is a pathway to understanding the former (Houze et al. 2006). TC structures comprise three main components: the eye, the eyewall, and the rainbands. Among these components, TC rainbands (TCRs) are the least understood because of their greater variations and infrequent sampling by weather radars. Existing observations and numerical simulations of TCs have yet to provide a comprehensive understanding of the full spectrum of TCRs. The role of TCRs in modulating TC intensity and their interactions with the eyewall are still open questions.

Radar and satellite observations have shown that TCRs are either stationary or moving with respect to the vortex center. A group of stationary TCRs, including the principal rainband, the secondary rainbands, and the connecting rainband, appears to maintain a fixed position relative to the vortex center and is therefore termed a stationary band complex (SBC; Willoughby et al. 1984). The principal rainband is a prominent member of SBC and is the most studied type of TCR (Barnes et al. 1983; Powell 1990a,b; May 1996; Hence and Houze 2008; Didlake and Houze 2009, 2013a,b;

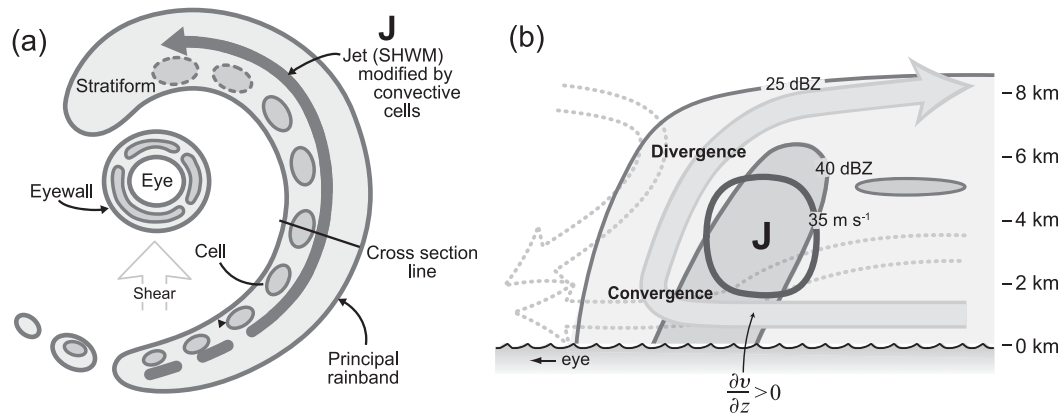*Corresponding author*: Xiaowen Tang, xtang@nju.edu.cn

FIG. 1. (a) The updated conceptual model of SBC and (b) the corresponding vertical structure of a principal rainband. [Adopted from Houze (2010) and Hence and Houze (2012).]

Tang et al. 2014). It has been shown that the principal rainband has the most active and frequent convection, compared to other types of TCRs (Willoughby et al. 1984; Houze 2010). Despite the prevalence of active convection, the conceptual model of SBC [Fig. 18 in Willoughby et al. (1984)] based on temporally averaged radar reflectivity only shows broader mesoscale structures. The principal rainband is historically depicted as a solitary and continuous precipitation band without convective-scale details. Partly because of the infrequent sampling and incomplete knowledge of the convective-scale details, the probable cause of principal rainbands has not yet been established (Houze 2010). Previously proposed theories (Willoughby et al. 1984; Riemer 2016) mainly focus on explaining the broader mesoscale features of the principal rainband by investigating the interaction of different dynamic and thermodynamic variables between the vortex core and the environment. Nevertheless, the convective-scale structure and dynamic characteristics of principal rainbands have yet to be understood (Riemer 2016).

The convective-scale structure is crucial for the understanding of not only the formation but also the dynamic role of principal rainbands because convection is the primary mechanism by which TCRs impact the local circulation. Previous studies have shown that the downdrafts associated with strong convection in TCRs are able to modify the subcloud layer (Barnes et al. 1983) and trigger new convection at the upwind end (Didlake and Houze 2009). The low-level supergradient jet of rainband convective cells could enhance the radial outflow above the boundary layer and create a circulation similar to the secondary eyewall (Didlake and Houze 2013a). The updraft is effective in redistributing mass and PV that may lead to the formation of a mid-level jet (Hence and Houze 2008) or secondary eyewall

(Judt and Chen 2010). The stratiform precipitation associated with convection is able to generate substantial wind maxima within a couple of hours (May and Holland 1999; Franklin et al. 2006). Because of the prevalence of active and frequent convection, the principal rainband may play a more important role in the structure and intensity change of TCs, compared to other types of TCRs (e.g., secondary rainbands and distant rainbands).

Recent studies using high-resolution airborne radar observations (Hence and Houze 2008; Didlake and Houze 2009, 2013a,b; Tang et al. 2014) have provided insights on the convective-scale structures of the principal rainband. As shown in the updated conceptual model of SBCs (Fig. 1a; Houze 2010), individual convective cells are embedded along the inner edge of the principal rainband and show characteristic intensity variations. The convective cells at the upwind end are in their developing stage, while the cells at the downwind end are decaying into a region of stratiform precipitation. In the middle portion, the cells reach their mature stage and display characteristic updraft and downdraft features, as shown in Fig. 1b. It is noted that the principal rainband in this updated conceptual model is still a solitary and continuous precipitation band directly composed of individual cells. Nevertheless, previous studies (May 1996; Hence and Houze 2008) have suggested that there might be different organizational modes of convection in the principal rainband. May (1996) showed that the principal rainband in TC Laurence (1990) appears to be organized at two distinct scales. Ground-based radar images show repetitive convective lines (subbands) formed at regular intervals within the principal rainband. Deep and active convection was confined to these subbands and formed a barrier to the radial inflow. Hence and Houze (2008) also

noticed a similar subband structure in the principal rainband of Hurricane Katrina (2005). The existence of the subband structure in different principal rainbands suggests that it may be an intrinsic mode of convective organization of principal rainbands and is supported by certain convective-scale dynamics, in addition to those proposed for the entire principal rainband (Willoughby et al. 1984; Riemer 2016). Because of the limited observations available in previous studies, the detailed structure, origin, and dynamic implication of such subbands are yet to be revealed.

In this paper, the subband structure within the principal rainband of Typhoon Hagupit (2008) is documented using the high-resolution National Science Foundation (NSF)–National Center for Atmospheric Research (NCAR) Electra Doppler Radar (ELDORA; Hildebrand et al. 1994) on board a U.S. Naval Research Laboratory (NRL) P-3 aircraft. The ELDORA repeatedly observed the most convectively active region of the principal rainband of Hagupit, possessing multiple distinct subbands in the radar reflectivity field. Two of these subbands were sequentially observed twice, about 1 h apart, by ELDORA. Tang et al. (2014) documented the structure and dynamics of one convective segment that contains multiple intense and upright convective cells with maximum vertical velocity >30 m s^{-1}. The multiple aircraft passes and dual-Doppler radar analyses provided a unique opportunity to investigate the detailed structure, origin, and dynamic impact of these subbands in the principal rainband of Hagupit. The rest of this paper is organized as follows. Section 2 gives a brief introduction of data and methods used in this study. Section 3 shows the structure, environmental characteristics, and origin of the subbands. Section 4 discusses the possible dynamic impact of the observed subbands. A summary and discussion are given in section 5.

2. Data and methodology

The high-resolution airborne dual-Doppler radar observations targeting the principal rainband of Typhoon Hagupit (2008) were collected during The Observing System Research and Predictability Experiment (THORPEX) Pacific Asian Regional Campaign (T-PARC) and Tropical Cyclone Structure 2008 (TCS-08) experiment (Elsberry and Harr 2008). A detailed description of Typhoon Hagupit (2008) during this field campaign can be found in Bell and Montgomery (2010) and Tang et al. (2014). During the time of the aircraft mission, Typhoon Hagupit had a maximum wind radius of ~60 km and a maximum surface wind speed of ~46 m s^{-1}. The flight track of the NRL P-3 between 0010 and 0510 UTC 22 September
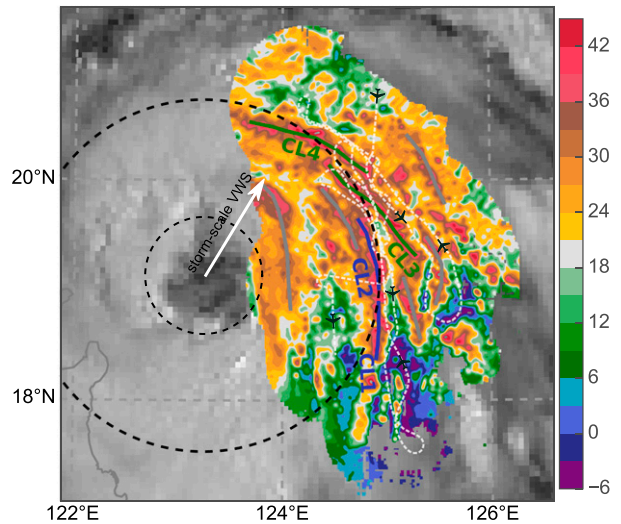

FIG. 2. The composite reflectivity at 3-km altitude during 0010–0510 UTC, observed by ELDORA, overlaid on the visible satellite image at 0245 UTC. The two circles represent the radius and 3 times the radius of the maximum surface wind at 0000 UTC. The white dotted line shows the flight track of the NRL P-3 starting from the upper-right corner. The gray, blue, and green lines show the axis of the convective lines, and the blue and green lines are analyzed in this study. The white arrow shows the direction of storm-scale vertical wind shear at 0000 UTC.

2008 superimposed on the composite ELDORA reflectivity at 3-km altitude is portrayed in Fig. 2. A notable feature of the aircraft observation in this mission is that instead of trying to survey the entire TC inner-core structure by using a "4" flight pattern (Marks and Houze 1984; Hence and Houze 2008), the NRL P-3 focused on the intense convection in the principal rainband by flying parallel to it.

The quality control, preprocessing, retrieval, and postprocessing procedures applied to the airborne radar observations are identical to those used in Tang et al. (2014). The ELDORA data were corrected for navigation errors (Testud et al. 1995; Bosart et al. 2002) and were processed via automated scripts to remove nonmeteorological artifacts, followed by interactive editing to clean up remaining artifacts using the NCAR Soloii software (Bell et al. 2013). Variational wind (Gamache 1997) and thermodynamic (Roux et al. 1993) retrievals were performed in a Cartesian grid with a 0.5-km resolution in both horizontal and vertical directions. The resulting three-dimensional wind, reflectivity, and thermodynamic fields in the Cartesian grid are interpolated into a storm-centered cylindrical coordinate system. The storm center and motion are determined using the Joint Typhoon Warning Center (JTWC) best track data. Typhoon Hagupit headed steadily in a north-northwest direction toward 330° at ~6.8 m s^{-1} during the flight mission.
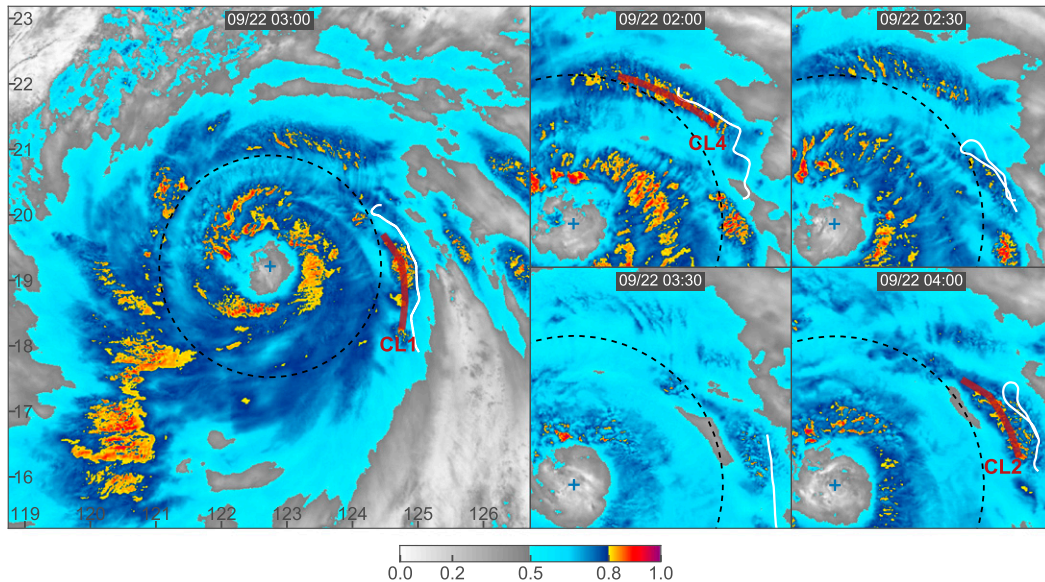
FIG. 3. Visible satellite images from *MTSAT-1R* during the aircraft mission. Albedo ≥ 0.8 is color enhanced to highlight the intense convection. The dashed circle represents 3 times the radius of maximum surface wind at 0000 UTC. The white lines are the flight tracks of ELDORA ± 30 min around the satellite observation time.

3. Structure and origin of subband

a. Structure characteristics of subband

The composite ELDORA reflectivity of the principal rainband at 3-km altitude over the 5-h period (Fig. 2) shows that the strong and isolated reflectivity (i.e., active convection) is organized into multiple subbands. The subbands are also evident in the visible channel satellite images (Fig. 3) from *Multifunctional Transport Satellite-1R* (*MTSAT-1R*), where thick clouds with albedo ≥ 0.8 are color enhanced to highlight the intense convection. It is noted that there are inner rainbands radially inside the subbands observed by ELDORA (e.g., the left panel). These inner rainbands will not impact the following analysis because they are mostly beyond the maximum observation range (70 km) of ELDORA. Despite the apparent existence of multiple subbands revealed by EL-DORA and *MTSAT-1R*, the microwave satellite image shows only a solitary, continuous rainband that fits various descriptions of a principal rainband [see Fig. 4c in Tang et al. (2014)]. There are a total of eight identifiable segments in Fig. 2, and four of them were used in this study. It is noted that some of the segments are actually the same subband observed at different times as Hagupit's center moved ~120 km toward 330° during the 5-h on-station time of the NRL P-3. These outward-moving convective subbands appear to reach maximum intensity at a preferred radius belt, where the optimal state of convection is more likely to be achieved (Tang et al. 2014), and then dissipate as they exit this belt.

Four quasi-straight segments (representing two subbands) in the aircraft mission are illustrated by the composite reflectivity fields at 3-km altitude superimposed on the visible satellite images individually (Fig. 4). It is clear that each segment possessed similar linear convective structures. The characteristic length and width of these segments are ~140 and 20 km, respectively, which are comparable with those documented in May (1996). However, the length and width of the entire principal rainband shown by the microwave satellite image (Fig. 3d; Tang et al. 2014) are ≥ 350 and ≥ 50 km, respectively. These subbands seem to be long lived (at least ≥ 1 h) and are clearly identifiable in the reflectivity composite (Fig. 2). Both the ELDORA reflectivity composite (Fig. 4) and the visible satellite images (Fig. 3) indicate that the subbands move downwind azimuthally and outward radially.

The 1-h interval between sampling different segments is not suitable to track the life cycle of individual convective cells, but it is adequate to investigate the variation/evolution of the structures of individual subbands. In the updated conceptual model (Fig. 1a), the convection in the principal rainband tends to be more intense in the upwind direction and weaker in the downwind direction. For the purpose of discussion, the four segments in Fig. 4 are labeled as CL1–CL4, according to their azimuthal locations from upwind to downwind relative to Hagupit's center rather than chronologically. It is noted that CL1, CL2 and CL3, CL4 are two subbands observed at different times. These subbands will be investigated by their averaged convective structure, which is constructed by
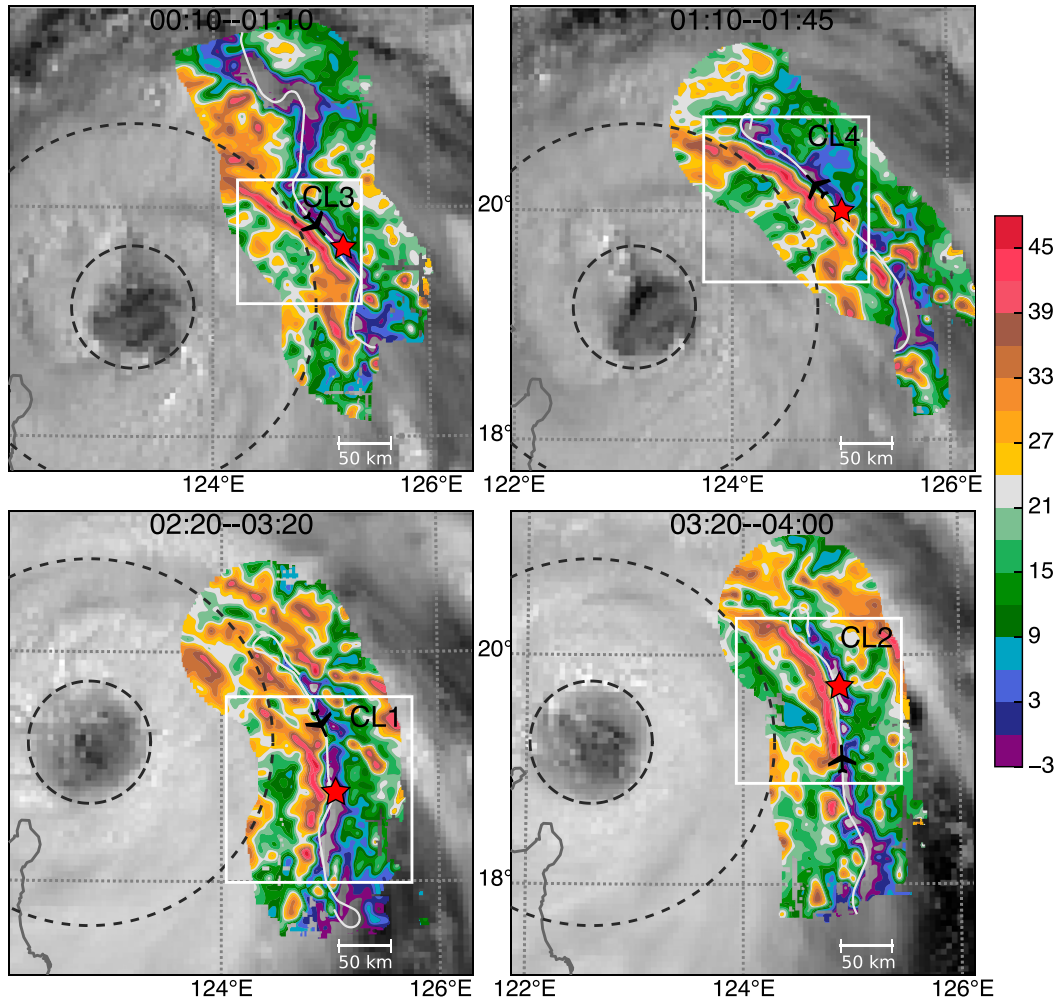
FIG. 4. As in Fig. 2, but for each quasi-straight flight leg. The white boxes show the region of dual-Doppler wind retrieval for each flight leg. The red stars show the locations of four dropsondes deployed by the NRL P-3.

averaging multiple (with an azimuthal interval of 1°) radial cross sections along the subband. A convective–stratiform separation algorithm (Didlake and Houze 2009) is first applied to find the boundary of the convective region of each segment. Each radial cross section then extends 25 km outward and 35 km inward from the center of the convective region.

1) VERTICAL VELOCITY

Figure 5 shows the along-band averaged vertical velocity of each segment superimposed on the reflectivity field. The updrafts and downdrafts are averaged separately to avoid canceling each other out (Didlake and Houze 2009). Segments observed at different times possess similar and coherent average structures, indicating a nontransient nature of these subbands. The main updrafts and downdrafts correspond well with the reflectivity cores. The updraft cores in CL1 and CL2 show a

displacement between the upper and lower levels, with the upper core (above 5-km altitude) on the inner side of the lower core (below 5-km altitude). There are two branches of downdraft. The weaker branch is outside of the updraft core at the upper level (above 10 km). The stronger branch is located in the inner side of the updraft core below ~10-km altitude. Although the general downdraft structures resemble those documented in Didlake and Houze (2009), the radial positions of the upper and lower downdrafts relative to the reflectivity core are different.

The updraft cores in the four segments are all elevated, indicating the existence of intense convection. The intensity of convection is comparable in CL1 and CL2, but it is stronger in CL3 than in CL4 in terms of the magnitude and height of the updraft core. When different subbands are compared, the second subband (CL3 and CL4) is weaker than the first one (CL1 and CL2).
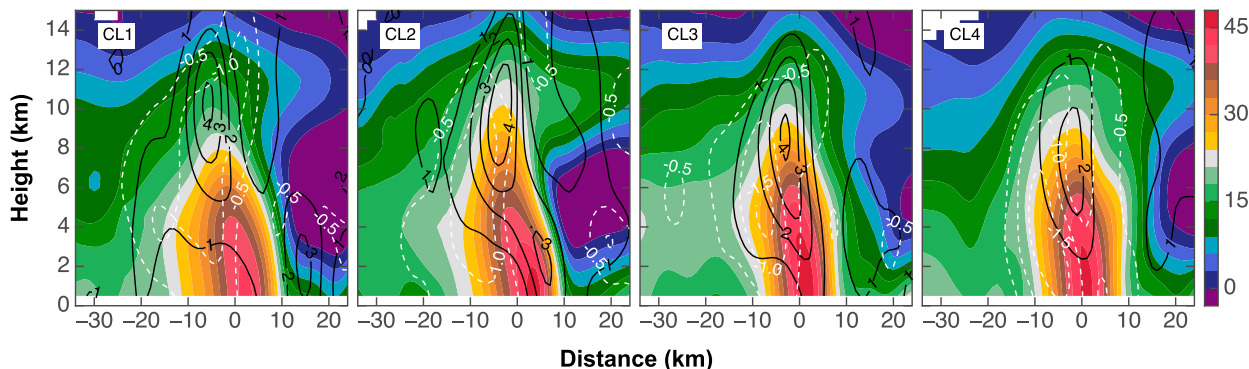
FIG. 5. Vertical velocity (contour) overlaid on the reflectivity (color) averaged along the subbands. Updraft (solid black) is contoured every $1\,\mathrm{m\,s^{-1}}$ starting at $1\,\mathrm{m\,s^{-1}}$, and downdraft (dashed white) is contoured every $0.5\,\mathrm{m\,s^{-1}}$ starting at $-0.5\,\mathrm{m\,s^{-1}}$. The left side of the abscissas is closer to the storm center.

The intensity of convection can be also estimated by the standard deviations (SDs) of the reflectivity field because the precipitation associated with intense convection is more inhomogeneous (Hence and Houze 2012). Figure 6 shows that the subbands possess an SD maximum at ∼5-km altitude near the melting layer. Above this level, the SD decreases rapidly, which reflects microphysical regimes dominated by ice processes (Hence and Houze 2012). The first subband (CL1 and CL2) has greater SD values compared to the second subband (CL3 and CL4) over the entire vertical extent, which is consistent with the relative intensity of convection derived by vertical velocity.

The statistical distribution of the vertical velocity is compared with those of previous studies (Lucas et al. 1994; May and Rajopadhyaya 1999) on tropical convective systems. As shown in May and Rajopadhyaya (1999), the mean and strongest 10% vertical velocities in different tropical convective systems are similar but significantly weaker than those over land. Comparably, TCRs have the weakest updraft and downdraft under 5-km altitude, with the strongest 10% updraft of $3\,\mathrm{m\,s^{-1}}$ and the strongest 10% downdraft of $-2.5\,\mathrm{m\,s^{-1}}$, respectively [Fig. 15 in May and Rajopadhyaya (1999)]. Figure 7 shows that the strongest 10% updraft and downdraft of the subbands under 5-km altitude are $>4\,\mathrm{m\,s^{-1}}$ and $\sim-4\,\mathrm{m\,s^{-1}}$, respectively. These values are significantly stronger than those in previously documented TCRs. The peaks of the strongest 10% updraft are found at ∼8 km in CL2 and CL3, which is consistent with the dual-Doppler-retrieved wind profile in Collis et al. (2013).

2) CROSS-BAND SECONDARY CIRCULATION

Figure 8 shows the along-band averaged secondary circulation (radial and vertical winds) of each segment. The secondary circulation shares similar structures at different times. The main updraft is rooted on the low-level

convergent zone mainly fed from the back (stratiform precipitation region) of the subband. This branch of radial outflow (which is inflow relative to the subband convection) may act as a partial barrier to the storm-scale inflow toward the eyewall and reduce the heat and moisture exchange between the vortex and ocean (Barnes et al. 1983; Powell 1990b). There is another branch of weaker, low-level inflow within 10 km outside the center of the convective region in CL1, CL3, and CL4. The apparent outflow outside 10 km of the center is likely affected by the boundary condition and the observation angle. The updraft splits into two branches at ∼8-km altitude. One branch veers toward the TC center, while the other branch continues to flow upward and turns outward at the upper levels. The structural features (e.g., the strong convection with trailing stratiform precipitation,
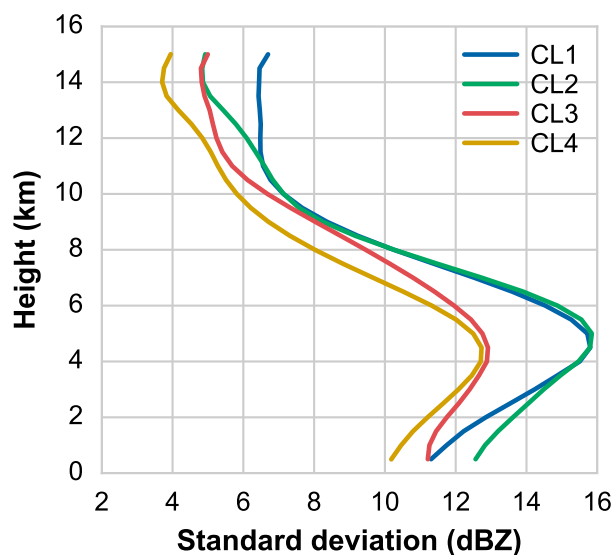

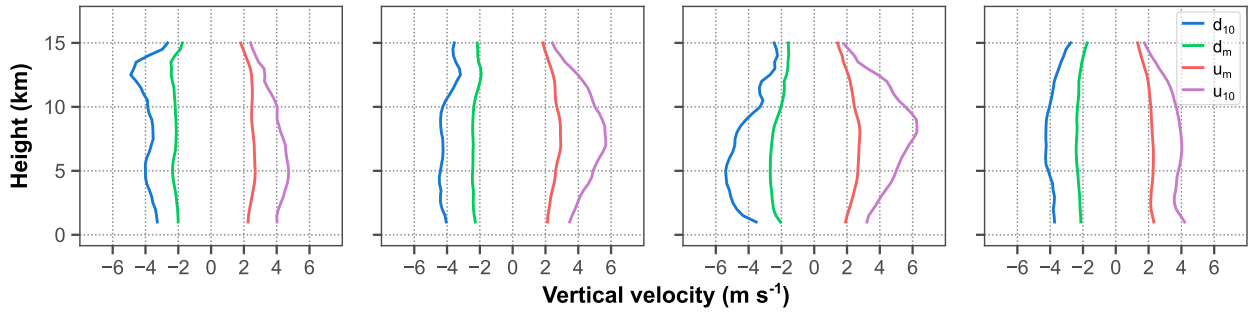FIG. 6. Vertical profiles of the SD of reflectivity for the four segments.

FIG. 7. The profiles of the mean and strongest 10% vertical velocities in the subbands. The distribution of updraft and downdraft is calculated separately. The labels d_{10}, d_m, u_m, and u_{10} represent the strongest 10% downdraft, the mean downdraft, the mean updraft, and the strongest 10% updraft, respectively.

the low-level descending outflow, and the midlevel inflow) resemble those of a typical midlatitude squall line (Houze et al. 1989) with trailing stratiform (TS) precipitation (Parker and Johnson 2000). The strong outflow at the upper levels, which is likely not part of the subband circulation but rather a storm-scale feature, is the main difference from the midlatitude squall lines. The squall-line-like flow field characteristics have been pointed out in Tang et al. (2014). The fact that all four segments show similar structures suggests that such characteristics are robust within Hagupit's principal rainband. It is noted that individual cross sections may not have all the flow features shown in Fig. 8 because convection is essentially three dimensional.

3) TANGENTIAL WIND

Figure 9 shows the along-band averaged tangential wind speed (only contours $\geq 24\,\mathrm{m\,s^{-1}}$ are shown) of each segment. The local tangential wind maximum (i.e., jet) is located on the inner side of the reflectivity core. This configuration is distinct from that depicted in the updated conceptual model (Fig. 1b), where the midlevel jet is on the outer side of the reflectivity core (e.g., Barnes

and Stossmeister 1986; Ryan et al. 1992; Samsury and Zipser 1995). Except for the different position relative to the reflectivity core, there is a branch of the jet extending to the lower levels. The intensity of the lower-level branch decreases from the first subband (CL1 and CL2) to the second one (CL3 and CL4), while the intensity of the midlevel branch increases from the first subband (CL1 and CL2) to the second one (CL3 and CL4). It is noted that because the four segments actually represent two subbands, the differences of the jet structure between segments can be attributed to the temporal evolution of individual subbands and to the band-to-band structural variation.

Though the radial position of the jet relative to the reflectivity core is apparently different than the conceptual model of principal rainbands constructed from previous case studies, the differences can be explained by the same dynamics. Recent numerical studies (Franklin et al. 2006; Moon and Nolan 2010; Li and Wang 2012) have shown that the acceleration of tangential wind in a TC-like vortex is the direct result of rainband heating. The convective heating is able to accelerate tangential wind at the lower and upper levels,
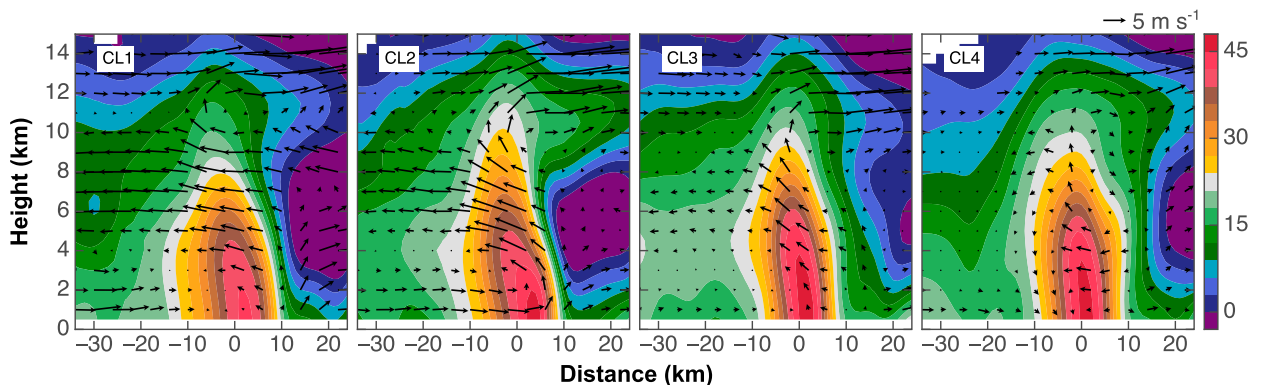

FIG. 8. Secondary circulation (radial and vertical velocity) overlaid on the reflectivity (color) averaged along the subbands.
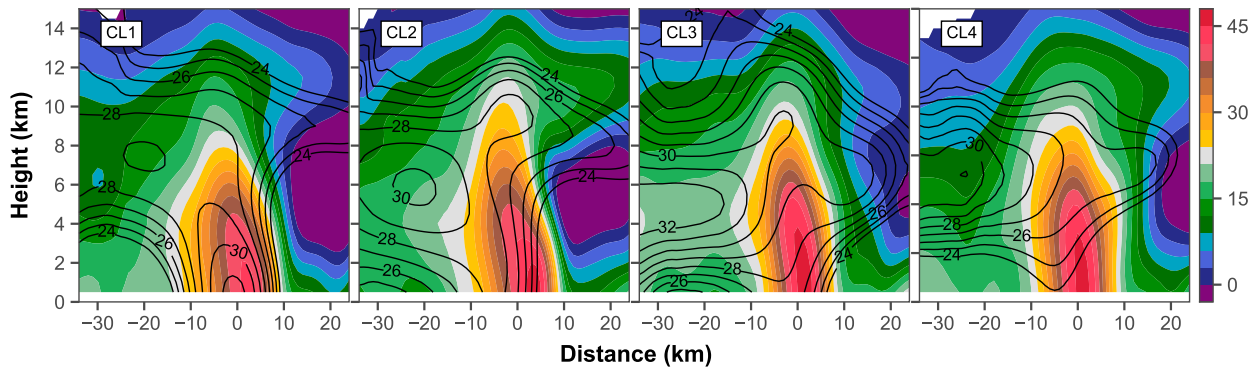
FIG. 9. Tangential wind speed (contour) overlaid on the reflectivity (color) averaged along the subbands. Only wind speed $>24\,\mathrm{m\,s}^{-1}$ is shown.

while the stratiform heating accelerates the tangential wind at the midlevels. The midlevel branch of the jet is on the same (inner) side of the reflectivity core as the stratiform precipitation, and the different intensities of the midlevel branch are probably related to the variations of the stratiform precipitation in different segments. Similarly, the lower-level branch of the jet can be attributed to the existence of active convection in the subbands. The intensity variations of the lower-level branch are consistent with those of the convection in different segments, as discussed in Figs. 5 and 6. It is noted that though the jet structure is consistent with different rainband heating in the above analyses, other dynamic effects (e.g., vertical advection of the tangential wind) of intense convection in TCRs could also lead to the similar structural variations of the jet (Didlake and Houze 2013a).

4) STRUCTURE VARIATION WITHIN SUBBANDS

The updated conceptual model in Fig. 1a shows developing convective cells at the upwind end of the principal rainband and decaying cells at the downwind end. It is worth noting that the four segments (CL1–CL4) are sequentially distributed along the downwind direction, while CL3 and CL4 are radially outward from CL1 and CL2 (Fig. 4). The intensity variation of these subbands in terms of their averaged structure is, in general, consistent with that of individual cells in the updated conceptual model. Because the subband itself is composed of convective cells and has a similar orientation to the principal rainband, it is interesting to investigate the intensity variation of cells within the subbands. Figure 10 shows the vertical velocity of the four segments at 10-km altitude overlaid on the reflectivity at 3-km altitude. There are intense updraft cores clustered in the downwind half of CL1, while strong updrafts are found at the upwind end of CL2. The overall updraft intensity is much weaker in CL3 and CL4

at the same altitude. There are a few strong updraft cores at the upwind end of CL3, but no significant updraft in the same region in CL4. In summary, the intensity of cells within individual subbands generally does not show the preference of stronger convection at the upwind direction and weaker convection at the downwind direction, despite that the averaged subband structure does.

b. Environmental conditions and origin of subband

Previous studies have shown that the storm-scale lower-level convergence (Willoughby et al. 1984) and vertical wind shear (VWS; Corbosiero and Molinari 2002; Hence and Houze 2012) are closely related to the distribution of convection in TCs. Convection is favored in the storm-scale convergent zone and the downshear right quadrant. Figure 11 shows the low-level (1000 hPa) divergence field using the ECMWF Year of Tropical Convection (YOTC) dataset (Waliser et al. 2012). This dataset has been widely used to study TCs and tropical convective systems (e.g., Yu and Cheng 2013; Xavier et al. 2015). The TC center, radius of maximum wind (RMW), and 3 times the RMW are shown as the black cross and circles. The vortex center is determined by a simplex algorithm that maximizes the axisymmetric tangential wind (Lee and Marks 2000; Bell et al. 2012). Figure 11 indicates that the location of the subbands only shows weak convergence. This is consistent with Riemer's (2016) result that the correspondence with the storm-scale convergence is not a critical factor for the existence of the principal rainband. The white arrow in Fig. 2 shows the environmental VWS calculated between 850 and 200 hPa (Didlake and Houze 2009). The location of the subbands is indeed on the downshear right quadrant, which is consistent with the statistical results shown in Hence and Houze (2012). However, the magnitude of $\sim$5 m s^{-1} is too weak, compared to the typical magnitude of VWS in which a preferred
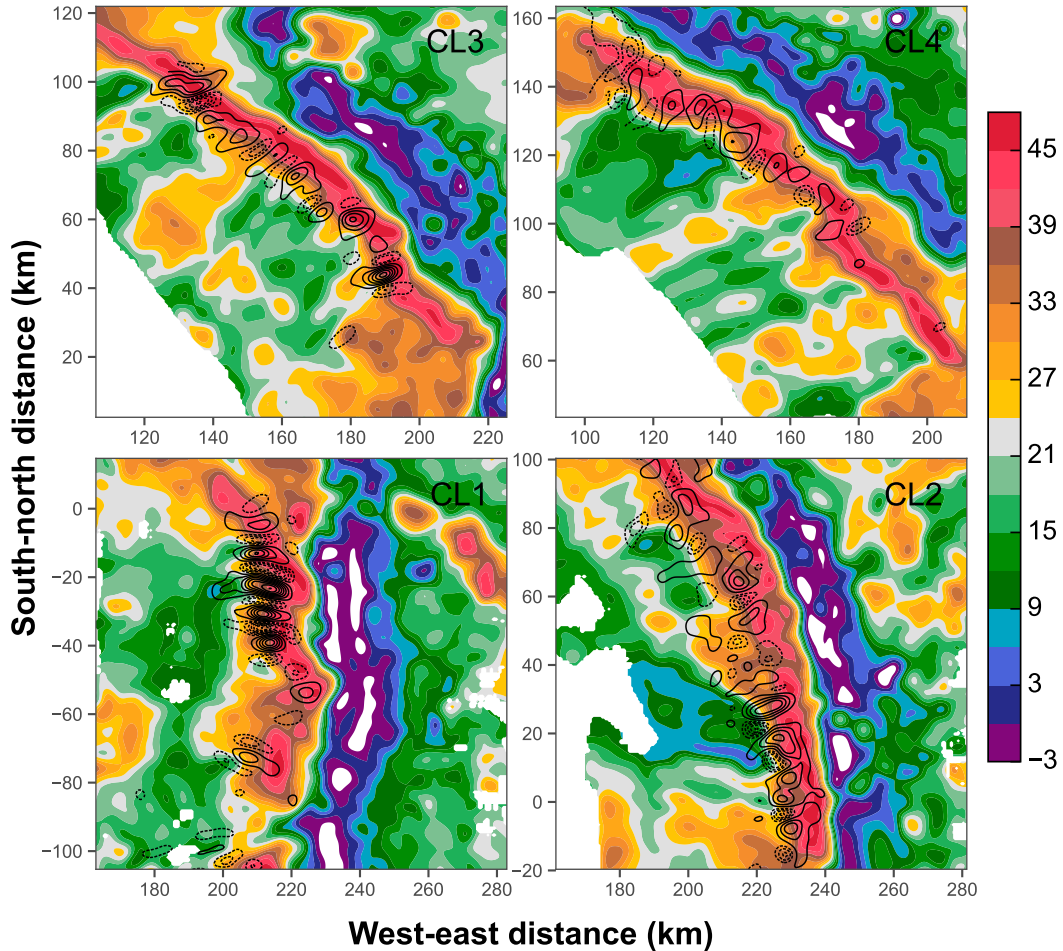
FIG. 10. The horizontal distribution of vertical velocity at 10-km altitude overlaid on the reflectivity at 3-km altitude for each convective segment. The displayed region is cropped, compared to the white box in Fig. 4, so that each panel has the same scale. The updrafts are contoured every $4\,\mathrm{m\,s^{-1}}$ starting at $2\,\mathrm{m\,s^{-1}}$, and the downdrafts are contoured $2\,\mathrm{m\,s^{-1}}$ starting at $-2\,\mathrm{m\,s^{-1}}$.

azimuthal distribution of convection is significant (Corbosiero and Molinari 2002).

The storm-scale dynamic factors are favorable for the development of convection in the approximate region of the subbands. However, they are not sufficient to explain the origin of the subbands because their horizontal scales are much larger than those of individual subbands. Willoughby (1977) postulated that inertial-gravity waves generated near the eyewall may be responsible for the origin of TCRs. However, the horizontal wavelengths of the simulated TCRs are too short to match observed TCRs. May (1996) noticed that the spacing of the simulated TCRs is close to that of the observed convective lines (subbands) in TC Laurence (1990). A simple analysis suggests that inertial-gravity waves are supported by the storm, and the characteristics of its second internal mode are consistent with the observed convective lines. Because the subbands in this

study resemble the convective lines in May (1996), a similar wave analysis is conducted. The storm-relative moving speed of the subbands is $\sim3\,\mathrm{m\,s^{-1}}$ outward and $\sim4.5\,\mathrm{m\,s^{-1}}$ cyclonically [Fig. 4 in Tang et al. (2014)], and the local 2–6-km mean wind is $\sim30\,\mathrm{m\,s^{-1}}$ from the dropsondes. Combining the two velocities gives an estimation of the phase speed of $\sim25.6\,\mathrm{m\,s^{-1}}$. The horizontal wavelength λ_x of the subbands is estimated to be $\sim50\,\mathrm{km}$, based on the left panel in Fig. 3. The Brunt–Väisälä frequency N is estimated to be $\sim0.01\,\mathrm{s^{-1}}$, based on the DOTSTAR dropsonde [Fig. 10 in Tang et al. (2014)]. According to May (1996), the estimated phase speed is

$$c = \frac{16\times10^3}{2\pi}\frac{N}{n} = \frac{25.5}{n}, \tag{1}$$

where n is the nth mode of the inertial-gravity wave, and the number 16 is the estimated depth (km) of the
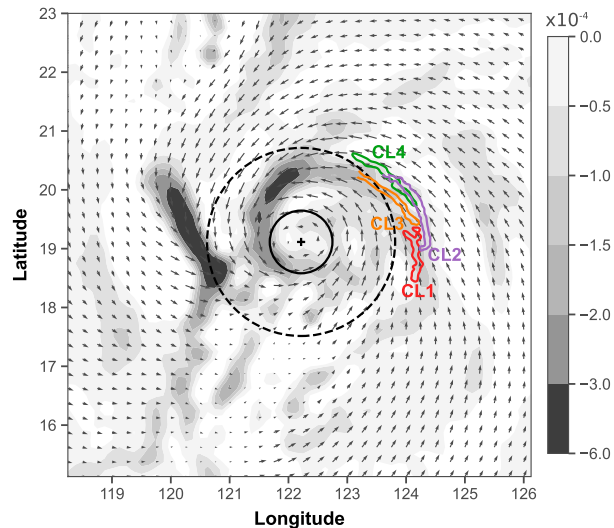
FIG. 11. The storm-scale divergence field (1000 hPa) at 0600 UTC 22 Sep 2008 from the ECMWF YOTC dataset. The cross (+) shows the storm center in the analysis field. The two circles represent the RMW and 3 times the RMW from the best track dataset. The color contours show the location of the subbands relative to the vortex center at the time of aircraft observation.

troposphere. The phase speed of the first internal mode ($n = 1$) given by (1) is ~25.5 m s^{-1}, which is close to the observed propagation speed of ~25.6 m s^{-1}. The speed V and radius R of the maximum wind at the observation time are 46 m s^{-1} and 60 km, respectively. The allowed wave solutions are

$$n < \frac{16 \times 10^3}{\sqrt{2}} \frac{N}{\lambda_x} \frac{R}{V} \approx 3, \qquad (2)$$

which suggests that the $n = 1$ mode is a possible solution. Because of the moving nature of the airborne radar, it is not feasible to further estimate and verify the period of the subbands. Nevertheless, the above analyses suggest that the inertial-gravity wave is a possible mechanism to explain the origin of the subbands. High-resolution numerical studies are still required to verify this hypothesis.

Although the inertial-gravity wave is a possible mechanism for the origin of the subbands, the subsequent development of the subbands is determined by their interaction with the environment. The structural resemblance to TS squall lines suggests that the subbands may exist in a similar environment to that of TS squall lines and are controlled by similar dynamics. According to Parker and Johnson (2000), the TS squall lines are commonly associated with more unstable local environments. Figure 12 shows the skew T–log$p$ diagrams of four dropsondes outside the subbands (the locations are marked by the red stars in Fig. 4). These dropsondes

were released from 3-km altitude (~700 hPa) by the NRL P-3. The upper part of the profiles in Fig. 12 is extended by a DOTSTAR dropsonde, assuming the upper atmosphere is less variable than the lower levels. The convective available potential energy (CAPE) values of these profiles are 1827, 1451, 2056, and 1771 J kg^{-1}, respectively, which are considerably larger than those in other principal rainbands (e.g., May 1996). Except for the large CAPE values, the environment is also conducive to the initialization of convection with little convective inhibition (CIN) of 3.9, 6.0, 0.1, and 0.2 J kg^{-1}, respectively. These small CIN values support the inertial-gravity wave hypothesis because it takes less effort for a wave to trigger convection. The weaker downdrafts shown in Fig. 5 are consistent with the moderate downdraft CAPE (DCAPE) values of 430.3, 391.1, 391.1, and 410.9 J kg^{-1}, respectively. The existence of dry layers below 700 hPa in Fig. 12 indicates the impact of downdrafts associated with active convection, which could enhance the low-level cold pool.

The prominent structure and dynamics associated with the TS squall lines are the convectively generated cool pool and its interaction with the local VWS. Tang et al. (2014) conjectured that the convective line in the principal rainband of Hagupit was supported by the balance between the cold pool and local VWS. Figure 13 further shows the along-band averaged virtual cloud temperature perturbation of the four segments. There is a persistent negative perturbation (cold pool) at the lower levels (below 4 km) on the inner side of the reflectivity core in all four segments. The location of the cold pool corresponds well to that of the stratiform precipitation, which suggests that the cold pool likely resulted from the evaporative cooling of the stratiform precipitation. The intensity and structure of the cold pools vary among the segments. The temperature difference below 3-km altitude is estimated to be ~3, 1, 3, and 4 K for each subband. The different cold pool strengths may have impacts on the propagation speed and the maintenance of the subbands (Rotunno et al. 1988; Corfidi 2003). The equivalent VWS associated with the cold pools is estimated to be ~17, 10, 17, and 20 m s^{-1}, respectively. Compared to the NRL P-3 dropsondes (Fig. 12), the equivalent VWS is close to the observed VWS in the local environment. Despite the uncertainties in the retrieval of the temperature perturbation and the determination of the parameters of the cold pool, the quasi balance between the cold pool and local VWS in all four segments indicates that it is probably a robust dynamic characteristic associated with the subbands. The existence of the quasi-balanced state and the structural similarities to midlatitude TS squall
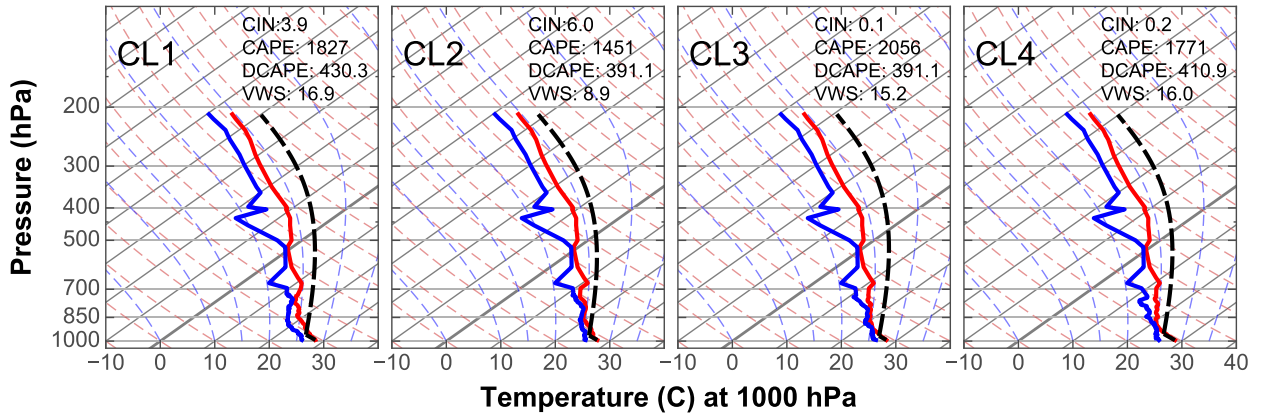
FIG. 12. Skew T–log$p$ diagrams of four dropsondes deployed near the four segments by the NRL P-3. The upper part (above 700 hPa) of the diagrams is extended using the profile from a DOTSTAR dropsonde.

lines strongly suggest that the cold pool dynamics proposed in Tang et al. (2014) controls the structural variations of the subbands.

4. Possible dynamic impact of subband

The similarity of structure, local environment, and dynamics portrayed in the last section suggests that the organization of convective cells into subbands is a robust feature of the principal rainband of Hagupit. Previous studies have suggested that diabatic heating (May and Holland 1999; Hence and Houze 2008) and secondary circulations (Barnes et al. 1983) in convective cells are possible mechanisms through which the TCR interacts with the vortex. Considering the prevalence of intense convection in the subbands, it is worthwhile to explore their impacts on the vortex. Limited by the available variables of the airborne radar observation, the possible impacts of the subbands are assessed by the vertical mass flux (VMF) and advection of absolute angular momentum (AAM).

a. Vertical mass flux

TCs are commonly conceptualized as regions of high potential vorticity (PV; Guinn and Schubert 1993). The variation of structure and intensity of a TC can be understood by its PV distribution. The total derivative of PV (Raymond and Jiang 1990) can be written as

$$\frac{dq}{dt} = \rho^{-1}\nabla \cdot (H\zeta_a + \theta\nabla \times F), \qquad (3)$$

where q is the potential vorticity, ρ is the air density, ζ_a is the absolute vorticity, H is the time rate of potential temperature θ, and F is the other forces (e.g., friction) applied per unit mass. Except for the layer close to the surface, the change of PV in a TC mainly results from the diabatic heating of convective and stratiform precipitation. Because of the intense convection in the subbands of Hagupit's principal rainband, stratiform precipitation behind the convection is highly attenuated in the ELDORA observations. Therefore, only the PV generation associated with the convection is discussed
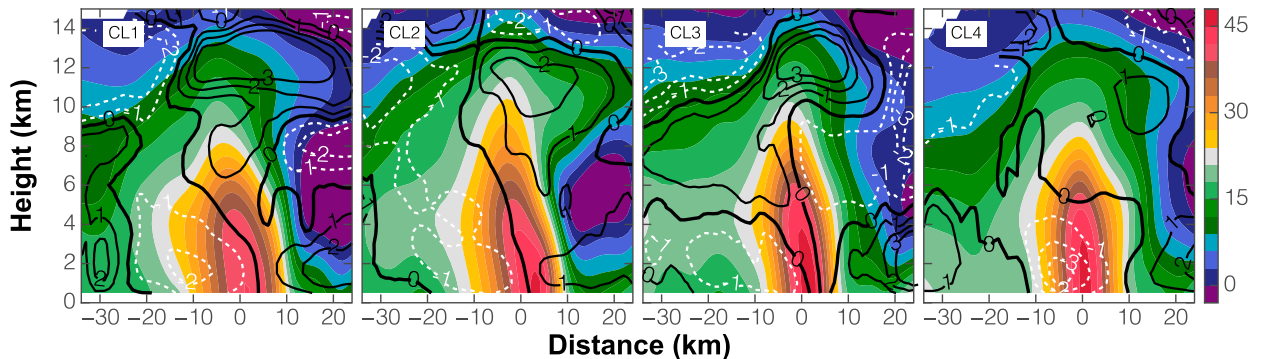

FIG. 13. Virtual temperature perturbation (contour) overlaid on the reflectivity (color) averaged along the subbands. Solid (black) and dashed (white) lines represent positive and negative values, respectively.
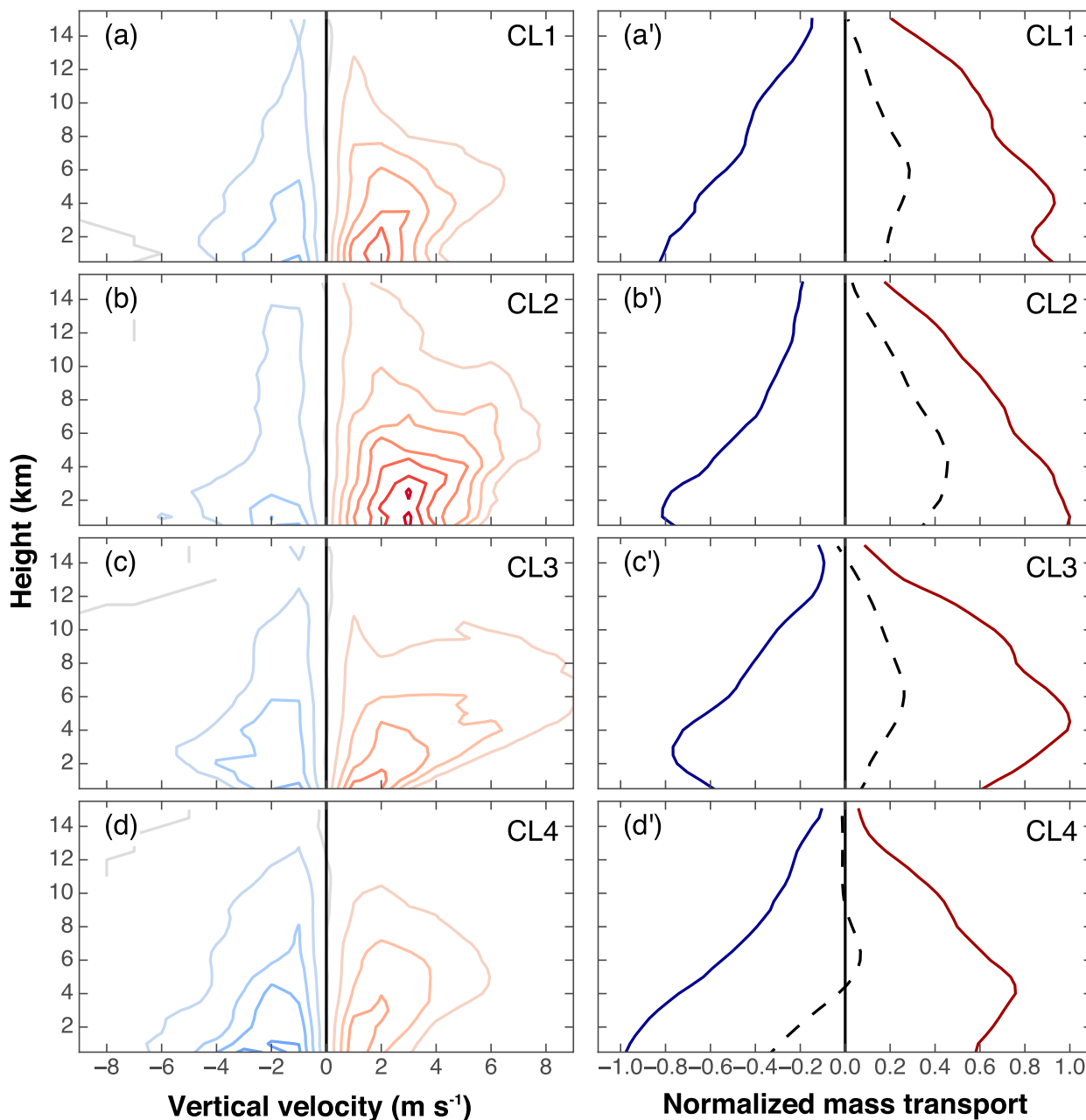
FIG. 14. (a)–(d) CFAD of VMF and (a′)–(d′) vertical profile of horizontally averaged VMF normalized by the maximum absolute VMF value of each flight leg. The CFAD is contoured every 5×10^{-2} kg s^{-1} m^{-2}.

below. Because diabatic heating is not directly measured from airborne Doppler radars, the heating rate from convection is approximated by (Raymond and Jiang 1990):

$$H = m\frac{\partial \theta}{\partial z}, \tag{4}$$

where $m = \rho w$ is the vertical flux of mass per unit area, and w is the vertical velocity. Assuming the lapse rate of potential temperature is constant in the convection region,

the vertical gradient of VMF can be used as a proxy to assess the contribution of TCR to PV distribution (Hence and Houze 2008).

Figure 14 shows the contoured frequency by altitude diagram (CFAD) of VMF per unit area (Figs. 14a–d) and the vertical profile of horizontally averaged VMF (Figs. 14a′–d′) of each segment. Figure 14a shows stronger upward VMF than downward VMF. The peak upward transfer comes from vertical velocity at 2 m s^{-1}, while the

peak downward transfer comes from $-1\,\mathrm{m\,s^{-1}}$. Both the averaged upward and downward VMF decrease with altitude, and the net VMF is upward throughout the vertical extent of the analysis region. The largest difference between the upward and downward VMF is near 6-km altitude. Figure 14b shows stronger upward VMF, which corresponds to the stronger updraft shown in Fig. 5b. The net VMF is also stronger and entirely upward in the analysis region, with a maximum value at 4-km altitude lower than that in CL1. Figure 14c shows reduced upward and downward VMF with a peak net value at $\sim$7-km altitude. The averaged upward VMF (Fig. 14c′) decreases rapidly below 5-km altitude. The upward VMF becomes weaker, and the downward VMF becomes stronger in CL4 (Fig. 14d) due to the weaker convection. The averaged net VMF is mainly downward below 4-km altitude, with a weak upward VMF at 4–8 km.

Barnes et al. (1991) documented a mature cell in a TCR of Hurricane Raymond (1983) that achieved an upward mass flux of $1.0 \times 10^8\,\mathrm{kg\,s^{-1}}$. It is estimated that 10–15 cells of this size and intensity can accomplish an upward mass flux equivalent to an eyewall of a moderate-intensity TC. The most convectively active region in the principal rainband of Hurricane Katrina (2005) achieved an upward mass flux of $18.0 \times 10^8\,\mathrm{kg\,s^{-1}}$ [K1 in Fig. 12 of Hence and Houze (2008)]. In the principal rainband of Typhoon Hagupit, the areal integrated upward mass flux of each segment is 9.8, 10.0, 6.1, and $5.5 \times 10^8\,\mathrm{kg\,s^{-1}}$, respectively. Considering the ubiquity and persistent nature of the subbands, they may have contributed significantly to the PV generation in Hagupit as it intensified from category 2 to category 3 during and after the aircraft mission. How exactly the PV generated by the subbands is related to the overall TC intensity change, however, cannot be explored in this dataset.

b. Advection of absolute angular momentum

The axisymmetric distribution of AAM in a TC typically increases with radial distance (Krishnamurti et al. 2005). Flow particles originated from outer radii carry higher AAM, which is either increased or decreased by various processes before they arrive at the eyewall. The intensity of a TC is collectively determined by the AAM of numerous such particles (Krishnamurti et al. 2005). In a cylindrical coordinate centered at a TC, the AAM can be expressed as

$$M = v_t r + \frac{f r^2}{2}, \qquad (5)$$

where v_t is the tangential wind, f is the Coriolis force, and r is the radial distance to the TC center. The possible impact of the subbands can be assessed by investigating

how AAM is modified in the subbands. The local change of AAM can be written as

$$\frac{\partial M}{\partial t} = -\mathbf{V}_h \cdot \nabla M - w \frac{\partial M}{\partial z} + \frac{\partial P}{\partial \theta} + F_\theta r. \qquad (6)$$

The four terms on the right-hand side of (6) are the horizontal and vertical advections of AAM, pressure, and friction torque. Previous studies (Pfeffer and Challa 1981; Molinari and Vollaro 1989) have shown that the upper-level AAM flux has an impact on TC intensity change. Recently, Martin and Krishnamurti (2011) showed that the midlevel horizontal advection of AAM is closely related to the intensity and strength changes of TCs. The intensifying TCs have larger horizontal advection of AAM located between 800 and 400 hPa and at radii outside 100 km. The location of the AAM advection suggests that it is likely associated with TCRs. For the convenience of discussion, the horizontal advection term is further divided into two terms:

$$-\mathbf{V}_h \cdot \nabla M = -\frac{v_t}{r} \frac{\partial M}{\partial \theta} - v_r \frac{\partial M}{\partial r}, \qquad (7)$$

where v_r is the radial wind speed. The terms on the right-hand side of (7) are the tangential and radial advection of AAM, respectively.

Figure 15 shows the along-band averaged radial advection of AAM for the four convective segments. There is a region of positive AAM advection at the midlevels on the inner side of the reflectivity core. The strength of this positive AAM advection is stronger in CL1 and CL2 and weaker in CL3 and CL4, which corresponds well with their averaged intensity of convection shown in Fig. 5. Because AAM typically decreases with radial distance ($\partial M/\partial r < 0$), the positive AAM advection mainly results from the strong midlevel inflow shown in Fig. 8. There are also regions of negative AAM advection located near the lower and upper outflow layers, which correspond to the radial outflows in Fig. 8. The along-band averaged tangential advection of AAM for the four segments shown in Fig. 16 is generally consistent with the structure of tangential wind speed shown in Fig. 9. The region of positive advection is found near the updraft and the midlevel inflow, and the negative advection is found near the upper levels in CL1 and CL2. The entire subband region shows positive tangential advection in CL3 and CL4. As shown by the animation from the Morphed Integrated Microwave Imagery (MIMIC; Wimmers and Velden 2007) product catalog, the principal rainband of Hagupit lasted more than 12 h. The cumulative effect of the AAM advection may have had significant impacts on the intensifying of Hagupit.

It is worth noting that although the potential vorticity redistribution and the advection of AAM in the subbands
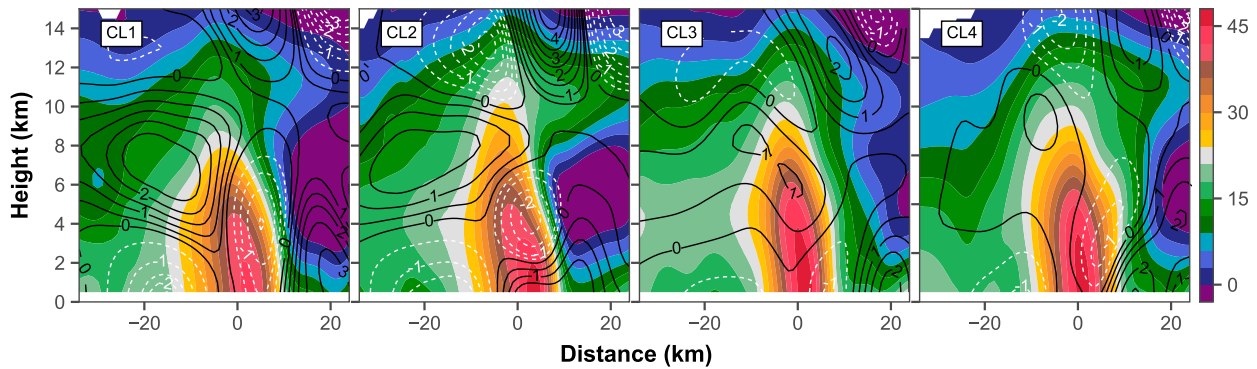
FIG. 15. Radial advection of AAM (contour) overlaid on the reflectivity (color) averaged along the subbands. The values are contoured every $0.5 \times 10^4 \, \text{m}^2 \, \text{s}^{-2}$ but labeled every $1 \times 10^4 \, \text{m}^2 \, \text{s}^{-2}$ for clarity.

both show positive impacts to the vortex, other negative impacts of convective structures in TCRs that are not discussed in this study are also possible. As mentioned in the analysis of Fig. 5, the strong low-level outflow in the subbands may act as a barrier and reduce the amount of heat and moisture available to the eyewall. The interaction between the inertial-gravity wave and the mean vortex may apply a "Reynolds torque" to slow down the mean flow (Willoughby 1977). The negative radial advection of AAM in Fig. 15 may also reduce the AAM of air parcels flowing to the eyewall and, consequently, reduce the vortex intensity.

5. Summary and discussion

This study examines the structure, origin, and dynamic impact of the subband structure in the principal rainband of Typhoon Hagupit. The principal rainband is evident as a solitary and continuous convective region in the microwave satellite image, while the airborne radar reflectivity field and visible satellite images identified multiple quasi-linear subbands in the same region. The

length and width of the subbands are smaller than those of the principal rainband shown by the microwave satellite image. The subbands are composed of active convection and trailing stratiform precipitation similar to the midlatitude squall lines. The updraft and reflectivity cores in the subbands are upright and elevated. The updrafts are mainly fed by the low-level outflow on the inner side of the convection and a weaker inflow on the outer side in some segments. The tangential wind speed shows a midlevel jet on the inner side of the reflectivity core that is likely accelerated by the heating of stratiform precipitation and a low-level jet that is attributed to the heating of convective precipitation. The secondary circulation in the radial cross sections shows characteristic flow patterns that are similar to those of TS squall lines in the middle latitudes.

The storm-scale convergence field and vertical wind shear are both favorable for the development of convection in the region of the subbands, but their horizontal scales are too large to explain the origin of the subbands. A wave analysis suggests that an inertial-gravity wave is supported by the vortex and is a possible
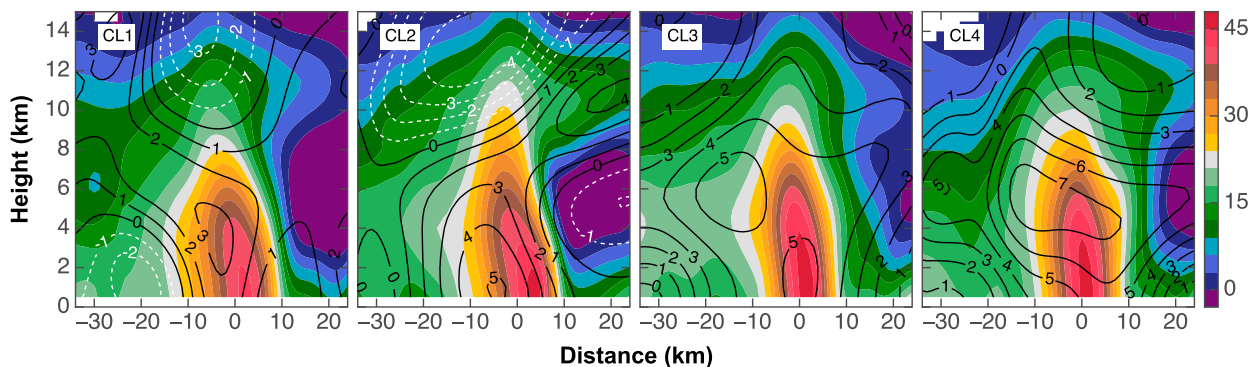

FIG. 16. Tangential advection of AAM (contour) overlaid on the reflectivity (color) averaged along the subbands. The values are contoured every $1 \times 10^4 \, \text{m}^2 \, \text{s}^{-2}$.

mechanism to explain the origin of the subbands. Four dropsondes deployed outside the subbands show that the local environment is characterized by little CIN, significant CAPE, and local VWS. These environmental factors are common ingredients for the development of TS squall lines, which is consistent with the squall-line-like structure of the subbands. The retrieved virtual cloud temperature further shows persistent negative perturbation at the lower levels, in the same region as the stratiform precipitation. The equivalent VWS estimated from the cold pool is close to that observed near the subbands. The quasi-balance state and the structural similarities to the TS squall lines suggest that the cold pool dynamics is likely the dominant factor controlling the structures of the subbands.

The intense and persistent nature of Hagupit's subbands suggests they may have had large impacts on the intensity change of Typhoon Hagupit. The possible impacts of the subbands are investigated in terms of PV generation and AAM budget. The PV generation is qualitatively assessed using the vertical gradient of VMF in convective regions as a proxy. The subbands observed at different times show different profiles of VMF consistent with their convective structures. The overall effect of these subbands accumulates PV at the lower levels, with a peak between 4- and 6-km altitude. The magnitude of the updraft VMF in the subbands is significant, compared with those in previous studies. The analysis of AAM reveals significant positive horizontal advection of AAM at the midlevels, which is closely related to the midlevel inflow of the secondary circulation in the subbands. Such positive advection may act to intensify the storm, according to previous numerical studies.

This study shows that the possible impacts of the subbands to the vortex are determined by specific structural characteristics (e.g., the vertical velocity profile and the midlevel inflow), and the relevant structures of the subbands are probably modulated by the local environment. It is worth pointing out that previously documented principal rainbands exist in storms at different stages of their life cycles. The local environment for the principal rainband could be very different in terms of dynamic and thermodynamic conditions. Consequently, principal rainbands found at different stages of TCs' life cycles or in different TCs may show different structures and play different roles in TC intensity changes. Because of the limitation of the observations and the complexity of the convective-scale structures, convective-permitting numerical studies are necessary to further understand the structural characteristics and dynamic impacts of the subbands as well as the principal rainband in general.

REFERENCES

Barnes, G. M., and G. J. Stossmeister, 1986: The structure and decay of a rainband in Hurricane Irene (1981). *Mon. Wea. Rev.*, **114**, 2590–2601, https://doi.org/10.1175/1520-0493(1986)114<2590:TSADOA>2.0.CO;2.

——, E. J. Zipser, D. P. Jorgensen, and F. D. Marks, 1983: Mesoscale and convective structure of a hurricane rainband. *J. Atmos. Sci.*, **40**, 2125–2137, https://doi.org/10.1175/1520-0469(1983)040<2125:MACSOA>2.0.CO;2.

——, J. F. Gamache, M. A. LeMone, and G. J. Stossmeister, 1991: A convective cell in a hurricane rainband. *Mon. Wea. Rev.*, **119**, 776–794, https://doi.org/10.1175/1520-0493(1991)119<0776:ACCIAH>2.0.CO;2.

Bell, M. M., and M. T. Montgomery, 2010: Sheared deep vortical convection in pre-depression Hagupit during TC S08. *Geophys. Res. Lett.*, **37**, L06802, https://doi.org/10.1029/2009GL042313.

——, ——, and W.-C. Lee, 2012: An axisymmetric view of concentric eyewall evolution in Hurricane Rita (2005). *J. Atmos. Sci.*, **69**, 2414–2432, https://doi.org/10.1175/JAS-D-11-0167.1.

——, W.-C. Lee, C. A. Wolff, and H. Cai, 2013: A solo-based automated quality control algorithm for airborne tail Doppler radar data. *J. Appl. Meteor. Climatol.*, **52**, 2509–2528, https://doi.org/10.1175/JAMC-D-12-0283.1.

Bosart, B. L., W.-C. Lee, and R. M. Wakimoto, 2002: Procedures to improve the accuracy of airborne Doppler radar data. *J. Atmos. Oceanic Technol.*, **19**, 322–339, https://doi.org/10.1175/1520-0426-19.3.322.

Collis, S., A. Protat, P. T. May, and C. Williams, 2013: Statistics of storm updraft velocities from TWP-ICE including verification with profiling measurements. *J. Appl. Meteor. Climatol.*, **52**, 1909–1922, https://doi.org/10.1175/JAMC-D-12-0230.1.

Corbosiero, K. L., and J. Molinari, 2002: The effects of vertical wind shear on the distribution of convection in tropical cyclones. *Mon. Wea. Rev.*, **130**, 2110–2123, https://doi.org/10.1175/1520-0493(2002)130<2110:TEOVWS>2.0.CO;2.

Corfidi, S. F., 2003: Cold pools and MCS propagation: Forecasting the motion of downwind-developing MCSs. *Wea. Forecasting*, **18**, 997–1017, https://doi.org/10.1175/1520-0434(2003)018<0997:CPAMPF>2.0.CO;2.

Didlake, A. C., and R. A. Houze, 2009: Convective-scale downdrafts in the principal rainband of Hurricane Katrina (2005). *Mon. Wea. Rev.*, **137**, 3269–3293, https://doi.org/10.1175/2009MWR2827.1.

——, and ——, 2013a: Convective-scale variations in the inner-core rainbands of a tropical cyclone. *J. Atmos. Sci.*, **70**, 504–523, https://doi.org/10.1175/JAS-D-12-0134.1.

——, and ——, 2013b: Dynamics of the stratiform sector of a tropical cyclone rainband. *J. Atmos. Sci.*, **70**, 1891–1911, https://doi.org/10.1175/JAS-D-12-0245.1.

Elsberry, R. L., and P. A. Harr, 2008: Tropical Cyclone Structure (TCS08) field experiment science basis, observational platforms, and strategy. *Asia-Pac. J. Atmos. Sci.*, **44**, 209–231.

Franklin, C. N., G. J. Holland, and P. T. May, 2006: Mechanisms for the generation of mesoscale vorticity features in tropical cyclone rainbands. *Mon. Wea. Rev.*, **134**, 2649–2669, https://doi.org/10.1175/MWR3222.1.

Gamache, J. F., 1997: Evaluation of a fully three-dimensional variational Doppler analysis technique. Preprints, *28th Conf. on Radar Meteorology*, Austin, TX, Amer. Meteor. Soc., 422–423.

Guinn, T. A., and W. H. Schubert, 1993: Hurricane spiral bands. *J. Atmos. Sci.*, **50**, 3380–3403, https://doi.org/10.1175/1520-0469(1993)050<3380:HSB>2.0.CO;2.

Hence, D. A., and R. A. Houze, 2008: Kinematic structure of convective-scale elements in the rainbands of Hurricanes Katrina and Rita (2005). *J. Geophys. Res.*, **113**, D15108, https://doi.org/10.1029/2007JD009429.

——, and ——, 2012: Vertical structure of tropical cyclone rainbands as seen by the TRMM Precipitation Radar. *J. Atmos. Sci.*, **69**, 2644–2661, https://doi.org/10.1175/JAS-D-11-0323.1.

Hildebrand, P., C. Walther, C. Frush, J. Testud, and F. Baudin, 1994: The ELDORA/ASTRAIA airborne Doppler weather radar: Goals, design, and first field tests. *Proc. IEEE*, **82**, 1873–1890, https://doi.org/10.1109/5.338076.

Houze, R. A., 2010: Clouds in tropical cyclones. *Mon. Wea. Rev.*, **138**, 293–344, https://doi.org/10.1175/2009MWR2989.1.

——, S. A. Rutledge, M. I. Biggerstaff, and B. F. Smull, 1989: Interpretation of Doppler weather radar displays of midlatitude mesoscale convective systems. *Bull. Amer. Meteor. Soc.*, **70**, 608–619, https://doi.org/10.1175/1520-0477(1989)070<0608:IODWRD>2.0.CO;2.

——, and Coauthors, 2006: The hurricane rainband and intensity change experiment: Observations and modeling of Hurricanes Katrina, Ophelia, and Rita. *Bull. Amer. Meteor. Soc.*, **87**, 1503–1521, https://doi.org/10.1175/BAMS-87-11-1503.

Judt, F., and S. S. Chen, 2010: Convectively generated potential vorticity in rainbands and formation of the secondary eyewall in Hurricane Rita of 2005. *J. Atmos. Sci.*, **67**, 3581–3599, https://doi.org/10.1175/2010JAS3471.1.

Krishnamurti, T. N., S. Pattnaik, L. Stefanova, T. S. V. Vijaya Kumar, B. P. Mackey, A. J. O'Shay, and R. J. Pasch, 2005: The hurricane intensity issue. *Mon. Wea. Rev.*, **133**, 1886–1912, https://doi.org/10.1175/MWR2954.1.

Lee, W.-C., and F. D. Marks, 2000: Tropical cyclone kinematic structure retrieved from single-Doppler radar observations. Part II: The GBVTD-simplex center finding algorithm. *Mon. Wea. Rev.*, **128**, 1925–1936, https://doi.org/10.1175/1520-0493(2000)128<1925:TCKSRF>2.0.CO;2.

Li, Q., and Y. Wang, 2012: Formation and quasi-periodic behavior of outer spiral rainbands in a numerically simulated tropical cyclone. *J. Atmos. Sci.*, **69**, 997–1020, https://doi.org/10.1175/2011JAS3690.1.

Lucas, C., E. J. Zipser, and M. A. Lemone, 1994: Vertical velocity in oceanic convection off tropical Australia. *J. Atmos. Sci.*, **51**, 3183–3193, https://doi.org/10.1175/1520-0469(1994)051<3183:VVIOCO>2.0.CO;2.

Marks, F. D., and R. A. Houze, 1984: Airborne Doppler radar observations in Hurricane Debby. *Bull. Amer. Meteor. Soc.*, **65**, 569–582, https://doi.org/10.1175/1520-0477(1984)065<0569:ADROIH>2.0.CO;2.

Martin, A., and T. N. Krishnamurti, 2011: The role of storm-relative advection of absolute angular momentum in strengthening of Atlantic tropical cyclones. *Geophys. Res. Lett.*, **38**, L19801, https://doi.org/10.1029/2011GL048910.

May, P. T., 1996: The organization of convection in the rainbands of Tropical Cyclone Laurence. *Mon. Wea. Rev.*, **124**, 807–815, https://doi.org/10.1175/1520-0493(1996)124<0807:TOOCIT>2.0.CO;2.

——, and G. J. Holland, 1999: The role of potential vorticity generation in tropical cyclone rainbands. *J. Atmos. Sci.*, **56**, 1224–1228, https://doi.org/10.1175/1520-0469(1999)056<1224:TROPVG>2.0.CO;2.

——, and D. K. Rajopadhyaya, 1999: Vertical velocity characteristics of deep convection over Darwin, Australia. *Mon. Wea. Rev.*, **127**, 1056–1071, https://doi.org/10.1175/1520-0493(1999)127<1056:VVCODC>2.0.CO;2.

Molinari, J., and D. Vollaro, 1989: External influences on hurricane intensity. Part I: Outflow layer eddy angular momentum fluxes. *J. Atmos. Sci.*, **46**, 1093–1105, https://doi.org/10.1175/1520-0469(1989)046<1093:EIOHIP>2.0.CO;2.

Moon, Y., and D. S. Nolan, 2010: The dynamic response of the hurricane wind field to spiral rainband heating. *J. Atmos. Sci.*, **67**, 1779–1805, https://doi.org/10.1175/2010JAS3171.1.

Parker, M. D., and R. H. Johnson, 2000: Organizational modes of midlatitude mesoscale convective systems. *Mon. Wea. Rev.*, **128**, 3413–3436, https://doi.org/10.1175/1520-0493(2001)129<3413:OMOMMC>2.0.CO;2.

Pfeffer, R. L., and M. Challa, 1981: A numerical study of the role of eddy fluxes of momentum in the development of Atlantic hurricanes. *J. Atmos. Sci.*, **38**, 2393–2398, https://doi.org/10.1175/1520-0469(1981)038<2393:ANSOTR>2.0.CO;2.

Powell, M. D., 1990a: Boundary layer structure and dynamics in outer hurricane rainbands. Part I: Mesoscale rainfall and kinematic structure. *Mon. Wea. Rev.*, **118**, 891–917, https://doi.org/10.1175/1520-0493(1990)118<0891:BLSADI>2.0.CO;2.

——, 1990b: Boundary layer structure and dynamics in outer hurricane rainbands. Part II: Downdraft modification and mixed layer recovery. *Mon. Wea. Rev.*, **118**, 918–938, https://doi.org/10.1175/1520-0493(1990)118<0918:BLSADI>2.0.CO;2.

Raymond, D. J., and H. Jiang, 1990: A theory for long-lived mesoscale convective systems. *J. Atmos. Sci.*, **47**, 3067–3077, https://doi.org/10.1175/1520-0469(1990)047<3067:ATFLLM>2.0.CO;2.

Riemer, M., 2016: Meso-β-scale environment for the stationary band complex of vertically sheared tropical cyclones. *Quart. J. Roy. Meteor. Soc.*, **142**, 2442–2451, https://doi.org/10.1002/qj.2837.

Rotunno, R., J. B. Klemp, and M. L. Weisman, 1988: A theory for strong, long-lived squall lines. *J. Atmos. Sci.*, **45**, 463–485, https://doi.org/10.1175/1520-0469(1988)045<0463:ATFSLL>2.0.CO;2.

Roux, F., V. Marécal, and D. Hauser, 1993: The 12/13 January 1988 narrow cold-frontal rainband observed during MFDP/FRONTS 87. Part I: Kinematics and thermodynamics. *J. Atmos. Sci.*, **50**, 951–974, https://doi.org/10.1175/1520-0469(1993)050<0951:TJNCFR>2.0.CO;2.

Ryan, B. F., G. M. Barnes, and E. J. Zipser, 1992: A wide rainband in a developing tropical cyclone. *Mon. Wea. Rev.*, **120**, 431–447, https://doi.org/10.1175/1520-0493(1992)120<0431:AWRIAD>2.0.CO;2.

Samsury, C. E., and E. J. Zipser, 1995: Secondary wind maxima in hurricanes: Airflow and relationship to rainbands. *Mon. Wea. Rev.*, **123**, 3502–3517, https://doi.org/10.1175/1520-0493(1995)123<3502:SWMIHA>2.0.CO;2.

Tang, X., W.-C. Lee, and M. Bell, 2014: A squall-line-like principal rainband in Typhoon Hagupit (2008) observed by airborne Doppler radar. *J. Atmos. Sci.*, **71**, 2733–2746, https://doi.org/10.1175/JAS-D-13-0307.1.

Testud, J., P. H. Hildebrand, and W.-C. Lee, 1995: A procedure to correct airborne Doppler radar data for navigation errors using the echo returned from the earth's surface. *J. Atmos. Oceanic Technol.*, **12**, 800–820, https://doi.org/10.1175/1520-0426(1995)012<0800:APTCAD>2.0.CO;2.

Waliser, D. E., and Coauthors, 2012: The "Year" of Tropical Convection (May 2008–April 2010): Climate variability and

weather highlights. *Bull. Amer. Meteor. Soc.*, **93**, 1189–1218, https://doi.org/10.1175/2011BAMS3095.1.

Willoughby, H. E., 1977: Inertia-buoyancy waves in hurricanes. *J. Atmos. Sci.*, **34**, 1028–1039, https://doi.org/10.1175/1520-0469(1977)034<1028:IBWIH>2.0.CO;2.

——, F. D. Marks, and R. Feinberg, 1984: Stationary and moving convective bands in hurricanes. *J. Atmos. Sci.*, **41**, 3189–3211, https://doi.org/10.1175/1520-0469(1984)041<3189:SAMCBI>2.0.CO;2.

Wimmers, A. J., and C. S. Velden, 2007: MIMIC: A new approach to visualizing satellite microwave imagery of tropical cyclones.

Bull. Amer. Meteor. Soc., **88**, 1187–1196, https://doi.org/10.1175/BAMS-88-8-1187.

Xavier, P. K., and Coauthors, 2015: Vertical structure and physical processes of the Madden–Julian oscillation: Biases and uncertainties at short range. *J. Geophys. Res. Atmos.*, **120**, 4749–4763, https://doi.org/10.1002/2014JD022718.

Yu, C.-K., and L.-W. Cheng, 2013: Distribution and mechanisms of orographic precipitation associated with Typhoon Morakot (2009). *J. Atmos. Sci.*, **70**, 2894–2915, https://doi.org/10.1175/JAS-D-12-0340.1.